R-38642

Reprinted from

theoretical and applied fracture mechanics

fracture mechanics technology

Theoretical and Applied Fracture Mechanics 22 (1995) 71–96

Characterization of strain-induced damage in composites based on the dissipated energy density
Part I. Basic scheme and formulation

P.W. Mast, G.E. Nash [1], J.G. Michopoulos *, R. Thomas [2], R. Badaliance, I. Wolock †

Mechanics of Materials Branch, Materials Science and Technology Division, U.S. Naval Research Laboratory, Washington, DC 20375, USA

ELSEVIER

ELSEVIER

Theoretical and Applied Fracture Mechanics 22 (1995) 71–96

theoretical and applied fracture mechanics

Characterization of strain-induced damage in composites based on the dissipated energy density
Part I. Basic scheme and formulation

P.W. Mast, G.E. Nash [1], J.G. Michopoulos *, R. Thomas [2], R. Badaliance, I. Wolock †

Mechanics of Materials Branch, Materials Science and Technology Division, U.S. Naval Research Laboratory, Washington, DC 20375, USA

Abstract

An approach to characterizing failure behavior and degree of load induced internal damage in composite materials and structures is formulated in Part I of this work. It is based on a systematic experimental procedure to observe the response of composite materials subjected to multiaxial load environment. The energy dissipated by internal failure mechanisms is employed as a measure of internal damage and is characterized by an energy dissipation function, which is identified by means of a deconvolution procedure using data provided by NRL's automated in-plane loader testing machine.

Part II of this work will display the dissipated energy density distributions in composite specimens that are used for the in-plane loader machine and naval structures, while Part III presents a general theory that includes the derivation for the constitutive behavior of the damaged composites.

1. Introduction

The use of composite materials in structural components has increased dramatically in recent years as their cost of production continues to decline and advances in composite design methodology become increasingly wide spread. As applications become more demanding, the need for reliable prediction of their mechanical properties and behavior is becoming ever more important.

The basic obstacle to a comprehensive understanding of failure behavior in composites is the sheer complexity of their observed mechanical behavior. Composites are generally anisotropic, markedly nonlinear, and, unlike metals, usually fail in an extremely complicated spatially diffuse noncatastrophic manner [1–3]. The nonlinear mechanical behavior of composites is known to be associated with damage accumulation which causes a local decrease in stiffness of the material in areas where damage is pronounced. In many fibrous composite systems, damage develops at applied loads much lower than the design limit [4]. For materials with a laminated structure, the

[1] Retired.

* Corresponding author. E-mail yiannis@prologos.nrl.navy.mil.

[2] Presently with FMT.

† Deceased.

0167-8442/95/$09.50 © 1995 Elsevier Science B.V. All rights reserved
SSDI 0167-8442(94)00050-6

complicated manufacturing process results in many imperfections that take on a variety of forms including fiber imperfections, fiber misalignment and geometrical irregularities in the distribution of fibers, voids or microcracks in the matrix material, and the presence of debonded areas. These defects, combined with high-stress fields near material or geometric discontinuities, induce matrix cracking, fiber breakage, fiber–matrix debonding, and delamination, all of which influence the overall mechanical properties of these materials. Extensive efforts [4–9] have been taken to identify the various modes of damage in composite materials in recent years. The primary outcome of these investigations was that macroscopic fracture was usually preceded by an accumulation of the different types of microscopic damage and occurred by the coalescence of this small-scale damage into macroscopic cracks. Moreover, it was generally found impossible to model the effects of the damage using analyses based on classical fracture mechanics approaches.

A more practical approach to modeling failure behavior in composites is to quantify the damage development on a continuum basis and relate it to the material constitutive behavior. The goal of such an approach is to permit accurate modeling of the progressive loss of stiffness and concomitant inelastic behavior due to the underlying micromechanisms of damage. Such modeling would represent an extremely important achievement from an engineering standpoint. For example, consider a laminated composite plate with a center hole made from a commercially available composite (i.e., AS1/3501-6 graphite/epoxy) that is loaded in quasi-static tension. Damage patterns will develop around the hole and near the corners of the plate [2] inducing degradation in material properties and forming a precursor to general failure. An examination of the micrographs readily indicates that a detailed micromechanical analysis is out of the question because the characteristic scale length of damage is of the order of μm leading to the conclusion that a continuum-based damage model would be far more appropriate under these circumstances.

The analysis of highly localized singular fields by means of continuum approaches has a long history and there exist a number of well-established techniques developed specifically for this purpose. Most of these approaches involve smearing out singular fields in some fashion and replacing them by locally homogeneous fields, an example being continuous dislocation theory [10,11]. More generally, there have recently been a plethora of continuum damage approaches based on the idea of an internal damage variable first introduced in [12–20]. A common shortcoming of most of these theories is that they are usually not based on observed facts, but rather tend to use models defined over low dimensional parameter spaces that reflect preconceived notions of the dominant failure mechanisms. Virtually no previous studies address this problem; indeed, this is one of the primary purposes of this work.

An appropriate model for composite failure behavior requires a large parameter space for its description if it is to represent a physical fact in a high-fidelity, objective manner. Because the phenomena being considered are generally so complex, it seems futile to formulate models in terms of the individual failure events; rather, the chosen model must be generic and phenomenological in nature and must rely on extensive sets of experimental data to identify the model parameters. Only after these parameters are determined can the model be related to particular failure mechanisms.

The proposed procedure involves the determination of an energy density dissipation function that has the dimensions of energy per unit volume and is postulated to be a property of the material. Its volume integral equals the energy dissipated during loading because of various internal failure events, and its value at any point in the material is regarded as a measure of load-induced internal damage. The energy dissipation function thus captures the collective behavior of these failure mechanisms without requiring an explicit knowledge of these mechanisms, and, moreover, can also be related to local stiffness changes which, as will be demonstrated subsequently, lead to a form of nonlinear structural behavior. In the sense that this material model relates load-induced internal damage to nonlinear structural behavior, it is similar to the models

recently used in [21–24]. The present approach is not limited to composites, but has application in the general area of the mechanics of irreversible processes where there is an acute need for a reliable and accurate procedure to experimentally determine equivalent dissipated energy density functions. This issue is more fully addressed in several works that deal with the thermomechanical modelling of irreversible processes associated with material behavior in general under mechanical loading [25–27].

Part I of this work describes the basic and computational scheme in determining the energy dissipation function. This function is determined from data obtained by means of an extensive series of tests performed with NRL's In-Plane Loader (IPL) [28–30]. This is a completely computer-controlled testing machine capable of producing multiple combinations of opening/closing, sliding, and rotating boundary displacements. Part II [31] will present the results for notched composite specimens and some Naval structures.

2. Basic scheme

The flow chart in Fig. 1 describes the basic scheme for determining the energy density dissi-

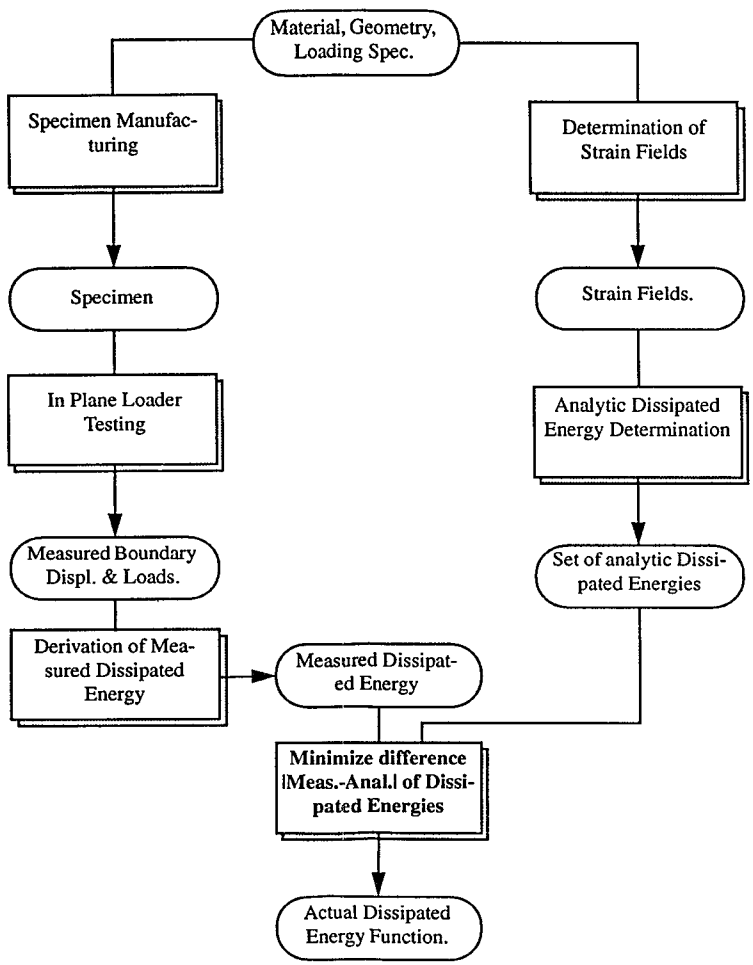

Fig. 1. Block diagram of processes involved in determining the dissipated energy function.

pation function by application of the IPL (In-Plane-Loader) tester and a computational procedure. The left subpath in Fig. 1 describes the experimental part of the identification process and basically involves determining the energy dissipated in the specimens. The initial step consists of using the material and geometry specifications to manufacture the test specimens. Next, the loading specifications are applied by using the IPL to load the specimens in the manner prescribed. Finally, the measured boundary displacements and loads are used to compute the total energy dissipated internally in the specimens due to strain-induced damage.

The remaining subpaths in Fig. 1 represent the numerical and analytical part of the process. Initially, as shown in the right subpath, the strain fields associated with each of the loading conditions prescribed in the loading specification are determined for the given material and specimen geometry. This is achieved by finite element analyses. A class of functions with free coefficients is then defined such that one member of this class can represent an analytic representation of the dissipated energy as a function of the strain fields. Finally, as indicated at the bottom of Fig. 1, the particular function that is best suited for representing the dissipation energy is computed by determining the values of the free coefficients that minimize the difference between the experimentally measured and the analytic representation of the dissipated energy.

The aforementioned procedure is a deconvolution procedure in the sense that the goal is to extract a material property (i.e., the dissipated energy density function) from information obtained from the material in a particular physical configuration, (i.e., the specimen), and thus, it is

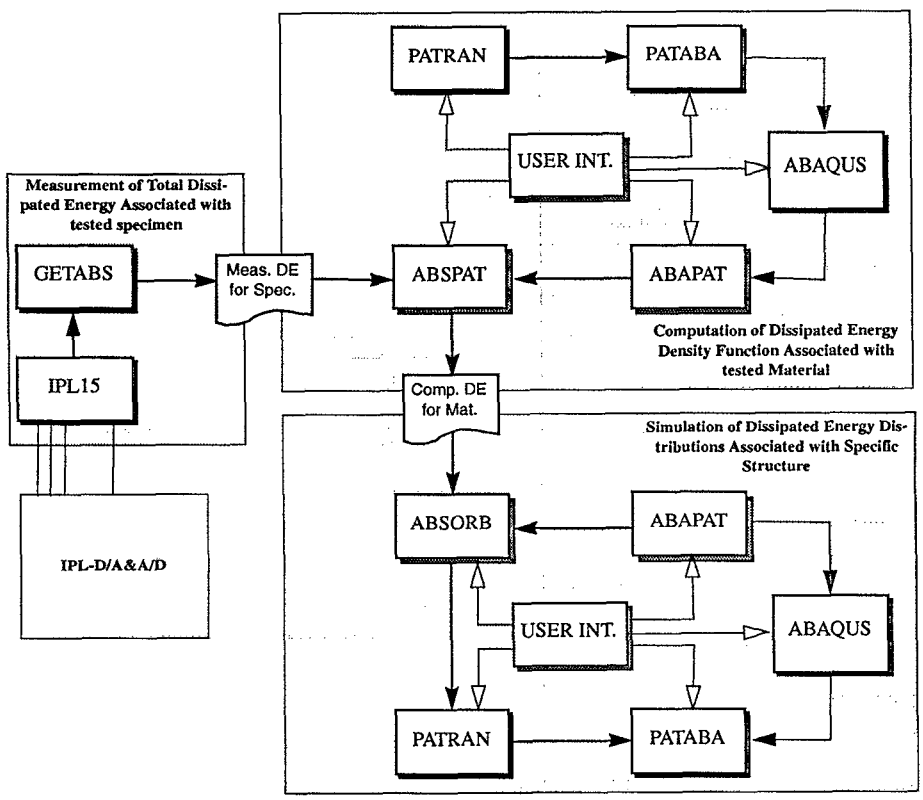

Fig. 2. Computational implementation of the current approach in terms of the essential modules and their functional relationship.

necessary to factor out specimen geometry effects.

The procedures in this approach have been implemented in a highly automated fashion by a sequence of computational activities that use the analyses described in the following sections. Fig. 2 shows a data flow diagram view of these processes and their relationships. The process of acquiring the IPL data and the computation of the measured total dissipated energy for the test specimen is described in Section 3, and is achieved through the processes "IPL15" and "GETABS," the latter of which evaluates the absorbed and dissipated energy in the specimen. Section 5 describes the computation of the dissipated energy density function. This is performed by

- using "PATRAN" to create the complete finite element model of the specimen,
- feeding the finite element data to the "ABAQUS" finite element code via the "PATABA" data translator,
- performing a linear elastic analysis to determine the strain field for each point in the specimen, and
- piping the measured dissipated energy of the specimen and the strain fields through the "ABAPAT" translators into "ABSPAT."
- "ABSPAT" then computes the dissipated energy density function by deconvolution and uses an optimization scheme to minimize the difference between the measured and the approximated values of the dissipated energy as described in Section 3.

Control of the interprocess and intercomputer communications is achieved through a user interface module.

The simulation of material stiffness loss over any particular structure as described in Section 2 of Part II [31] is achieved by

- using "PATRAN" to specify the finite element idealization and loading specification of the structure,
- piping the data to "ABAQUS" via the "PATABA" data translator to compute the strain fields associated with the selected loading conditions, and
- piping the computed dissipated energy density function and the strain field via the "ABAPAT" translator into "ABSORB" to obtain the dissipated energy distributions over the structure which can then be displayed using "PATRAN."

Again, control of the interprocess and intercomputer communications is achieved through another user interface module.

While the energy dissipation function can be approximately determined without explicit knowledge of the damage-induced constitutive nonlinearities as discussed above, a more refined approximation requires a representation of the full-scale nonlinear behavior. This information is also of much interest in its own right since it is needed for stress analysis when analyzing the behavior of structural components loaded well into the nonlinear response range where substantial load redistribution is expected. Part III addresses the development of a representation of the constitutive behavior in terms of the energy dissipation function along with a refined scheme for identifying the dissipation function itself.

3. Data acquisition through the in-plane loader system

3.1. Material

Composites associated with structural applications range through a wide variety of materials. Each different combination of matrix, fiber, fiber coating (for matrix-fiber interface), layup angle, stacking sequence, etc., corresponds to a different material. The approach is specifically tailored to organic matrix composites. In general, the particular material specification for an application in a structure depends not only on the mechanical considerations but also on a host of additional considerations such as cost, electromagnetic and thermal properties. Approximately 100 material systems with graphite fibers ranging from AS1 to IM7 (Hercules Corp.) and several thermoset and thermoplastic organic polymers have been tested and characterized with the present approach. Here the description is limited to the materials selected for the applications discussed in this paper. A brief description of these materials is

given in Table 1 in terms of the matrix, the fiber, and the angle of layup. Appendix A in [30] gives a complete list of all the materials tested.

Most of the materials were received in the form of panels out of which the specimens were cut and machined to the specimen specification.

Table 1
Fragment of the materials data base describing four of the materials utilized in the present study out of a total of 101 different materials

Item	Resin	Fiber	Layup	Supplier	File	Project
001	3501-6	AS1	+/−15	Hercules	mt-1	NAV-SEA
002	–	–	+/−30	–	mt-2	–
007	–	AS4	+/−60	–	mt-7	–
040	PEEK	–	+/−60	ICI	mt-40	–

3.2. Specimen

The specimen geometry shown in Fig. 3 was designed to satisfy the following requirements:

- The characteristic dimensions be large enough relative to fiber diameter and lamina thickness to ensure that the material could be analyzed as either a single mechanically equivalent homogeneous anisotropic monolithic material, or a collection of layers of varying orientations of such materials.
- The overall specimen size be small enough to keep material costs at a manageable level.
- A strain riser be present to guarantee that high-strain regions occur well away from all specimen boundaries.

Fig. 3 shows the single edge-notched specimen that resulted. It is important to note that the primary function of the notch is to act as a strain riser to ensure satisfaction of the last requirement above, and not to mimic a crack in the fracture mechanics sense.

3.3. Loading

The experimental system used for measuring the dissipated energy in the test specimens is the In-Plane Loader System (IPLS) [28,30]. The primary component of the IPLS is a custom-made, fully automated testing machine (IPL) shown in Figs. 4(a) and 4(b). The remaining components of the IPLS are a computer that fully controls the IPL and a graphics processor that is used for various postprocessing operations in conjunction

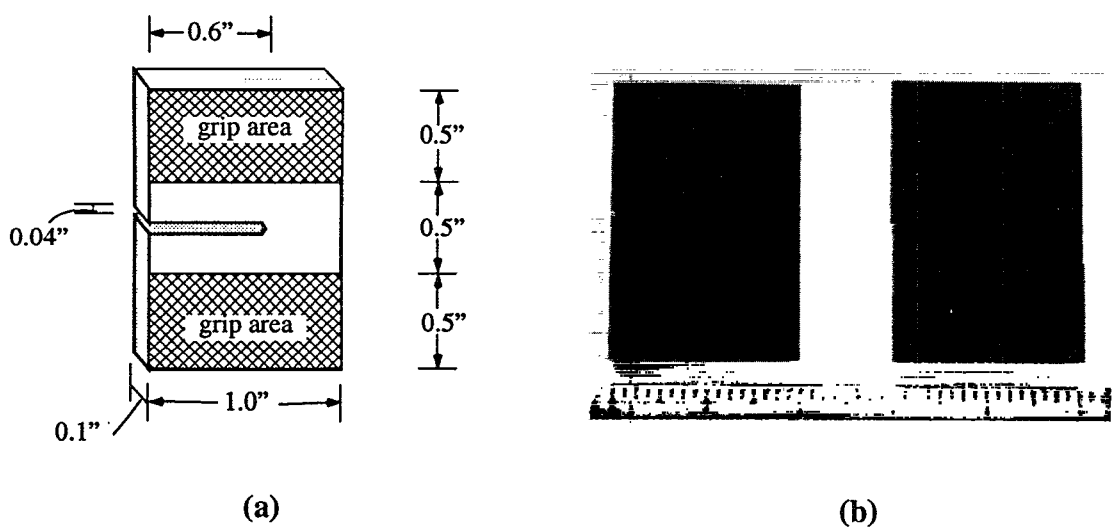

Fig. 3. (a) Schematic of the specimen and the associated areas. (b) Photos of representative specimen before testing (left) and after testing (right), for material 2 with 3501-6 resin AS1 fiber and +/−30° layup and loading path 11.

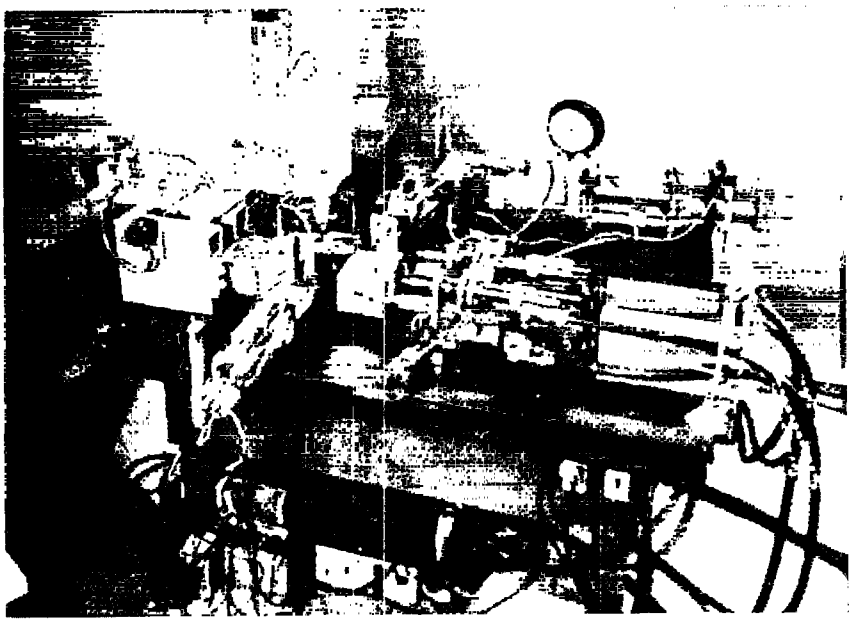

(a)

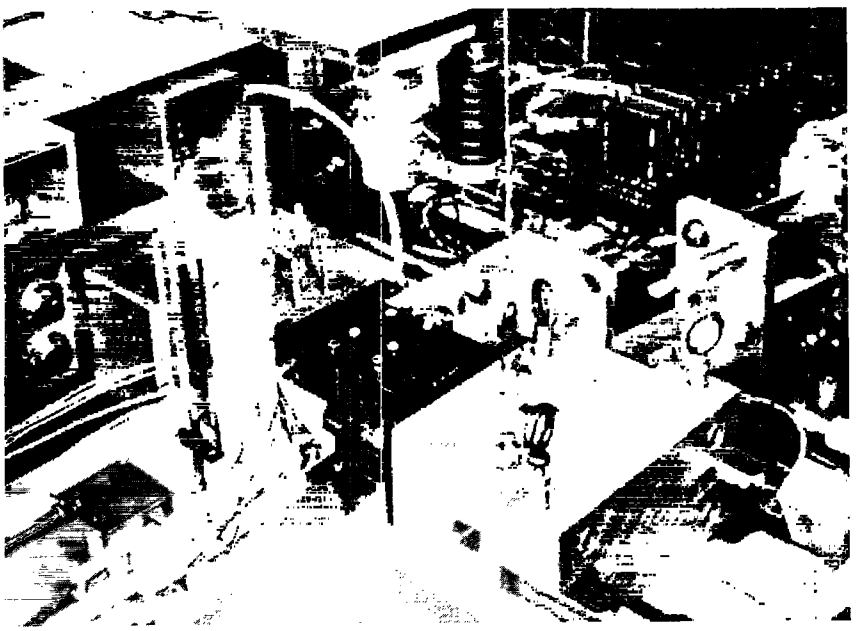

(b)

Fig. 4. (a) Side view of the in-plane loader. (b) View of the grip area of the in-plane loader.

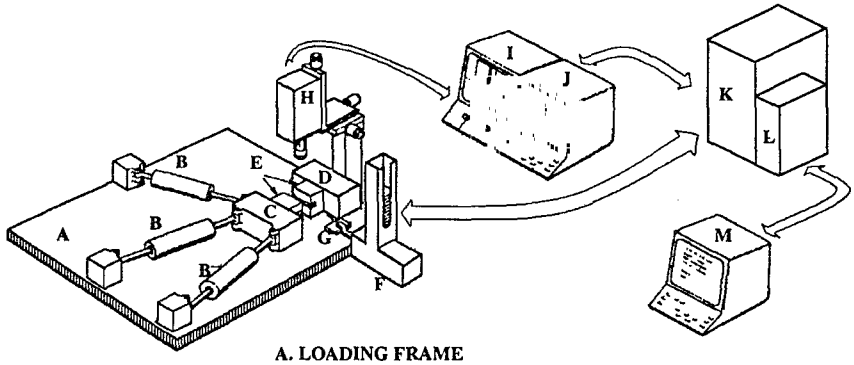

A. LOADING FRAME
B. HYDRAULIC ACTUATORS
C. MOVABLE HEAD
D. FIXED HEAD
E. SPECIMEN GRIPS
F. SPECIMEN LOADER/UNLOADER
G. TEST SPECIMEN
H. VIDEO CAMERA
I. VIDEO MONITOR FOR POSITIONING DEVICE
J. MAIN TERMINAL
K. COMPUTER
L. GRAPHICS PROCESSOR
M. GRAPHICS TERMINAL

Fig. 5. Schematic representation of the In-Plane Loader System.

with the computer system. A detailed description of this testing system can be found in Figs. 5 and 6. Refer to Appendix B in [30] for a description of the IPLS components. The objective of the IPLS is to control the rigid body motion of the boundary of the specimen that is held by the

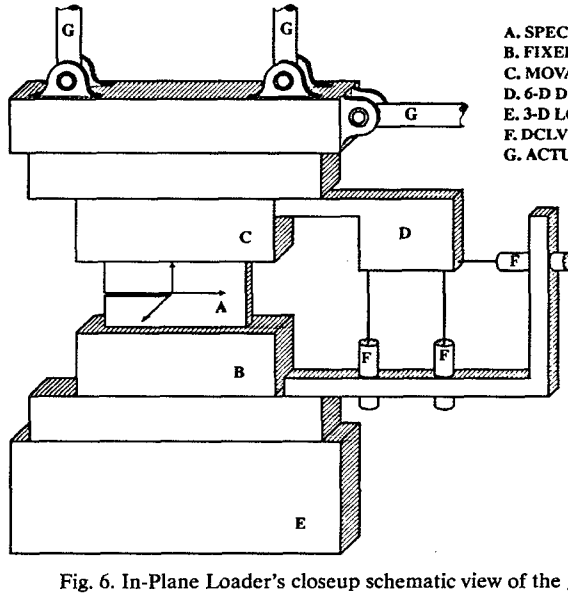

A. SPECIMEN
B. FIXED GRIP
C. MOVABLE GRIP
D. 6-D DCLVDT X/DUCER
E. 3-D LOADING CELL
F. DCLVDT
G. ACTUATOR

Fig. 6. In-Plane Loader's closeup schematic view of the grip area.

movable grip. Because the actuators are constrained to move in a plane parallel to the specimen, the resulting motion involves only three degrees of freedom relative to any frame of reference on that plane.

The relation between the prescribed actuator displacements and the resulting grip motion is illustrated in Figs. 7(a) and 7(b). It is important to note here is that the grip motion can be resolved into three basic components: sliding u_x, opening/closing u_y, and rotation ω. Specified combinations of actuator displacements, therefore, map into particular combinations of these three basic motions. It is convenient to use a reference frame located at the initial position of the notch tip for both the boundary displacements (denoted by $\boldsymbol{u}$ relative to this frame) and the resulting reaction forces $\boldsymbol{f}$. Fig. 7(c) illustrates these displacements and tractions and the resulting deformation of the specimen.

The decomposition of the applied displacements relative to this frame into a sliding motion u_0, an opening/closing motion u_1, and a rotational motion u_2 is shown in Figs. 7(d)–7(f) and Figs. 8(b)–8(d), respectively. For dimensional homogeneity, u_2 is defined as the length of the arc traveled by a point 1 in. away from the notch tip rigidly connected with the moving grip along the direction of the rotation, instead of using the actual rotation in radians. Subsequent analysis requires that computing the energy dissipated within the material at a discrete set of observation points as the specimen is loaded by applying a predetermined series of boundary displacements u^p. Here $p = 1 \cdots n$ and n denotes the number of observation points. It is advantageous to think in terms of a three-dimensional displacement space with coordinates (u_0, u_1, u_2). The issue then is how to select a representative family of paths that cover the space and how to sample along each path.

It is not expected to observe any significant path-dependent behavior during this initial loading phase. The mechanical response of the mate-

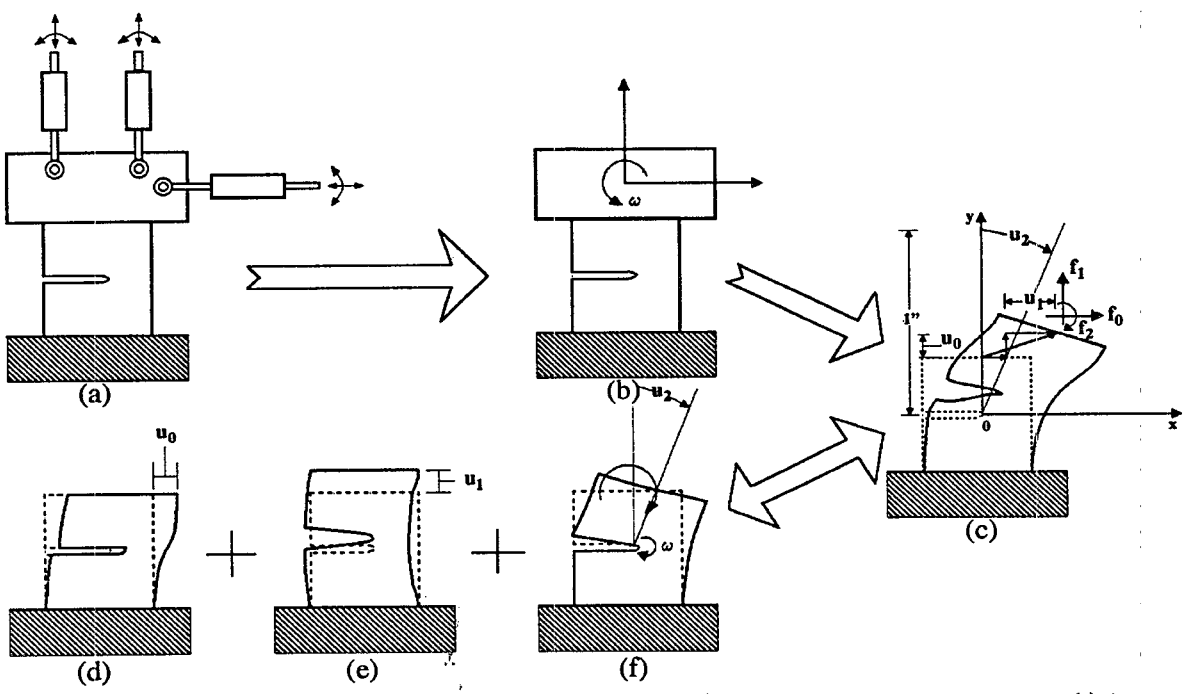

Fig. 7. Schematic of the equivalence between the (a) actuator motions and (b) the three modes of motion, as well as (c) the process of composing an arbitrary loading combination, from linear combinations of the three basic motions: (d) shear, (e) opening/closing and (f) rotation.

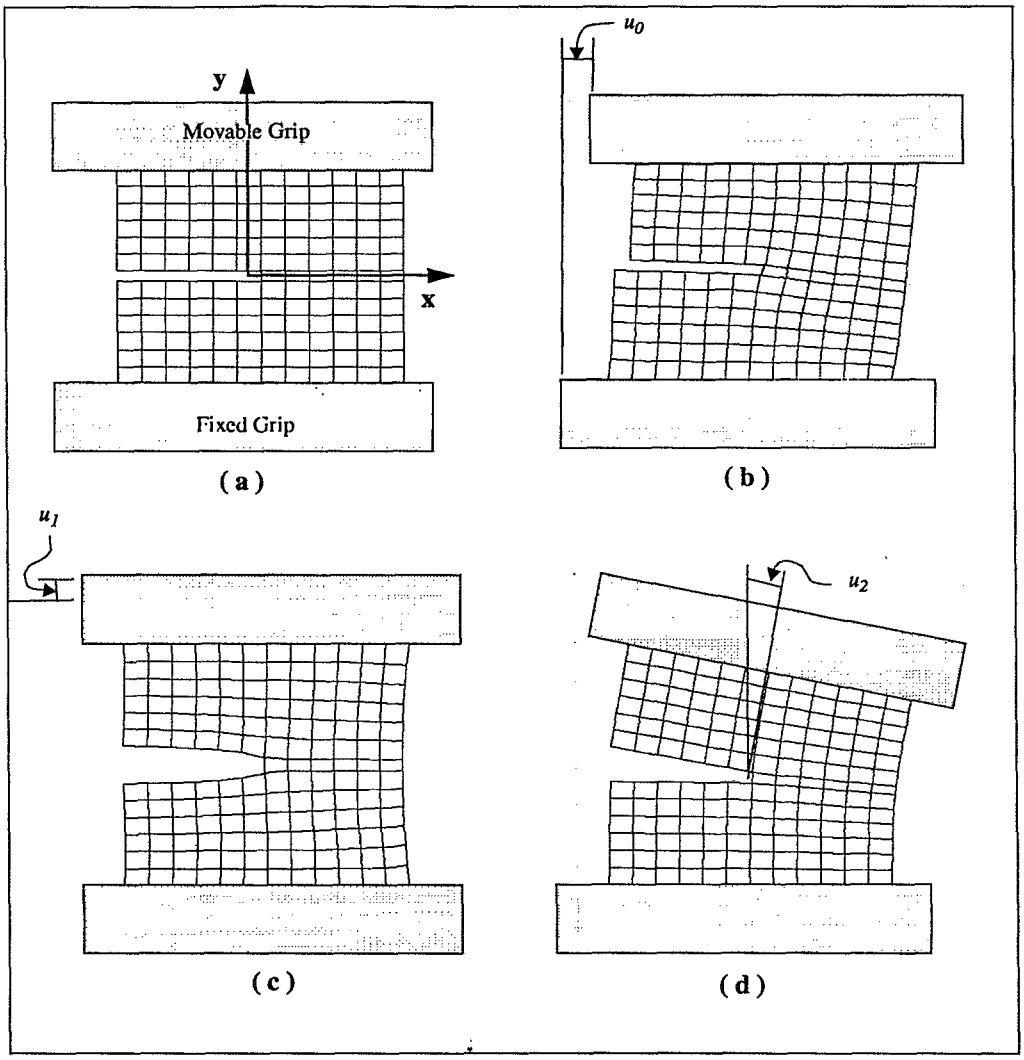

Fig. 8. View area of the IPL specimen in the grips before applying any loading (a), after applying some translation of the upper grip parallel to the x-axis (b), parallel to the y-axis (c) and after applying rotation about the origin of the x–y frame of reference (d).

rial at any point in this space is thus expected to depend only on the current state of internal strain and to be independent of the particular path followed to achieve this state. This type of path independence is consistent with the observations made in [33] and greatly simplifies matters because it permits us to cover the displacement space with a family of loading paths selected solely on the basis of convenience.

Towards this end, it was decided to cover the boundary displacement space with a set of 15 uniformly distributed radial loading paths as indicated in Fig. 9. Note that because of geometry and material symmetry about the x axis (Fig. 8(a)), only the half-space corresponding to positive sliding displacement ($u_0 > 0$) need be considered. The required set of observation points is generated by sampling along each path at 50

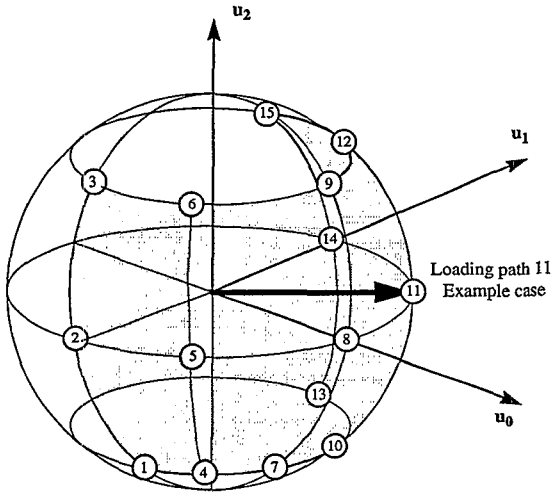

Fig. 9. Definition of the proportional loading paths in the boundary displacement space (loading path 11 is a representative case), and the uniform distribution of the 15 paths used in the present methodology.

distinct points starting from 0 mils and terminating at a maximum of 50 mils of displacement yielding a total of 750 points per material system. Then a particular test in that the actuator motions are continuously varied corresponds to a specific path in this space. This path can be represented by a vector originating from the origin of the space and components given by $u_i = ra_i$ for $i = 0, 1, 2$, where a_i are the coordinates of the unit vectors along the loading path direction, and r is a scalar multiple denoting the proportionality of the path and ranging from 0 to 0.05 in. in steps of 0.001 in. corresponding to the successive observation points. Only 15 specimens are required, and 50 observations per loading path are obtained from a single specimen. Table 2 shows the coordinates a_i of the unit vectors for the selected loading paths.

The locus of the end points of all loading paths for the same increment is a half-sphere as shown in Fig. 9, where loading path 11 at an arbitrary increment is presented as an example.

3.4. Testing procedure

The IPL is instructed to apply loads along the designated loading path for each specimen. Because each test is performed twice to establish the degree of reproducibility, 30 (2 per loading path) specimens are required for analyzing a single material. After the IPL calibration phase is complete, a stack of thirty specimens from the same material is loaded on the magazine of the automated specimen feeder of the IPL and the testing phase follows. The following sequence of events is repeated for each specimen.

- The specimen is fed from the specimen magazine into the grip area of the IPL.
- Pressure is applied on the hydraulic grips to clamp the specimen with the appropriate force to prevent slippage and crushing of the specimen.
- The operator uses the digital imaging system of the IPL to control the positioning of a crosshair on the image of the area between the grips as acquired by the overhead video camera. Notch tip location and selected points between the grips are thus automatically fed into the com-

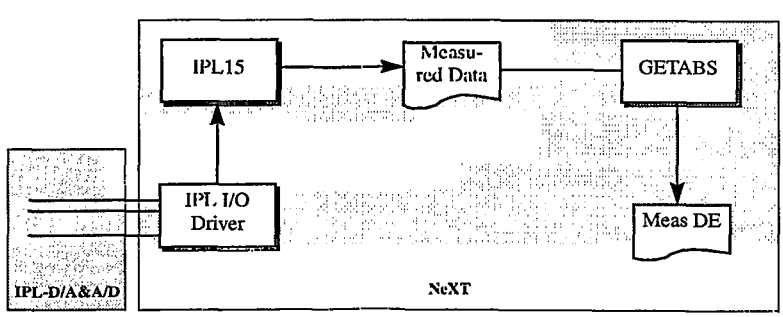

Fig. 10. Block diagram of the computational modules and resources involved with the determination of the measured total dissipated energy.

```
MT-2.ASC
__Date__.__Time__._Exptr__._Matrl__._Specnu_._Thick__._Grpopn_.Width__
10/20/87 13:31:44 MAST     AS1-30          34     0.143     0.594     0.462
_Tran-1_._Tran-2_._Polr-1_._Polr-2_._Polr-3_._Padthk_._Coefrc_.___N3___
   0.058    -0.369  -90.000  -45.000     0.050     0.192     0.250   100.000
_Fidc-1_._Fidc-2_._Lowr-1_._Lowr-2_._Notc-1_._Notc-2_.___N1___.___N2___
    7304      2040     13648     11184      8008      7720        50         1
No.Absorption.__Disp-X__.__Disp-Y__._Rotation_._Force-X__._Force-Y__._Moment___
 1  0.000E+00  0.000E+00  0.000E+00  0.000E+00  0.000E+00  0.000E+00  0.000E+00
 2  0.000E+00 -0.756E-05 -0.851E-04 -0.232E-04 -0.569E+00 -0.668E+00 -0.277E+01
 3 -0.186E-02 -0.118E-03  0.168E-03 -0.335E-03  0.151E+02 -0.502E+02 -0.137E+02
 4  0.192E-01 -0.750E-04 -0.385E-03 -0.110E-02  0.140E+02 -0.637E+02 -0.109E+02
 5  0.191E-01 -0.220E-03 -0.475E-03 -0.175E-02  0.151E+02 -0.906E+02 -0.116E+02
 6  0.142E-01 -0.374E-03 -0.473E-03 -0.236E-02  0.168E+02 -0.118E+03 -0.127E+02
 7  0.461E-01 -0.486E-03 -0.944E-03 -0.308E-02  0.132E+02 -0.146E+03 -0.581E+01
 8  0.209E-01 -0.634E-03 -0.923E-03 -0.371E-02  0.156E+02 -0.172E+03 -0.141E+02
 9  0.591E-01 -0.763E-03 -0.128E-02 -0.441E-02  0.171E+02 -0.198E+03 -0.635E+01
10  0.758E-01 -0.870E-03 -0.168E-02 -0.513E-02  0.185E+02 -0.225E+03 -0.941E+01
11  0.940E-01 -0.970E-03 -0.218E-02 -0.587E-02  0.195E+02 -0.253E+03 -0.164E+02
                          . . .
                          . . .
                          . . .
45 -0.404E+00 -0.109E-01 -0.105E-01 -0.290E-01  0.592E+02 -0.989E+03 -0.128E+03
46 -0.341E+00 -0.112E-01 -0.111E-01 -0.298E-01  0.579E+02 -0.101E+04 -0.138E+03
47 -0.771E+00 -0.118E-01 -0.108E-01 -0.304E-01  0.580E+02 -0.103E+04 -0.149E+03
48 -0.569E+00 -0.122E-01 -0.115E-01 -0.312E-01  0.580E+02 -0.106E+04 -0.155E+03
49 -0.648E+00 -0.126E-01 -0.118E-01 -0.319E-01  0.560E+02 -0.108E+04 -0.164E+03
50 -0.787E+00 -0.130E-01 -0.121E-01 -0.326E-01  0.557E+02 -0.110E+04 -0.179E+03
__Date__.__Time__._Exptr__._Matrl__._Specnu_._Thick__._Grpopn_.Width__
10/20/87 13:32:05 MAST     AS1-30          35     0.143     0.594     0.462
_Tran-1_._Tran-2_._Polr-1_._Polr-2_._Polr-3_._Padthk_._Coefrc_.___N3___
   0.058    -0.283  -90.000     0.000     0.050     0.192     0.250   100.000
_Fidc-1_._Fidc-2_._Lowr-1_._Lowr-2_._Notc-1_._Notc-2_.___N1___.___N2___
    7304      2040     13648     11184      8008      6388        50         1
No.Absorption.__Disp-X__.__Disp-Y__._Rotation_._Force-X__._Force-Y__._Moment___
 1  0.000E+00  0.000E+00  0.000E+00  0.000E+00  0.000E+00  0.000E+00  0.000E+00
 2  0.000E+00 -0.312E-04  0.193E-03  0.462E-04 -0.308E+00 -0.287E+00 -0.514E+01
 3  0.337E-02 -0.487E-05 -0.468E-05  0.671E-04 -0.947E+01 -0.400E+02  0.137E+02
 4  0.937E-02  0.188E-03 -0.355E-03  0.655E-04 -0.177E+01 -0.113E+03  0.119E+02
                          .
                          .
                          .
```

File Header

First Specimen Header

First Specimen Data

Second Specimen Header

Second Specimen Data

Fig. 11. Typical parts of file containing the measured through the in plane loader data.

puter of the IPLS, to establish the frame of reference.
- The remainder of the test is performed automatically, with the computer control system measuring specimen thickness and controlling the grip pressure, selecting and applying incrementally the loading path. The system monitors and stores the boundary forces and displacements for each loading step, and using this data the total energy dissipated in the specimen for each loading increment in the loading path is computed and stored along with the force displacement data.

3.5. Computational and data description

Fig. 10 is a data flow diagram showing the computational process corresponding to the left subpath of Fig. 1. The data from the A/D and D/A converters are directed to module "IPL15" through the input/output driver module. "IPL15" controls the data acquisition and control process by controlling the following operations:
- it controls the positioning of the actuators and the associated hardware;
- it collects the force and displacements (f, u) at the 50 sampling points along the loading path from the transducers;
- it then transforms them into those referring to the frame of reference attached on the tip of the notch as in Fig. 8(a);
- it computes and displays the total and instantaneous values of the total dissipated energy lost in the specimen due to damage;
- it finally stores all measured quantities in files (one per material). Here the term "material" is used for a laminate of specific fiber, matrix, and lamination angle.

Each file contains the data for all specimens and loading paths for a given material. Each file consists of a header and a series of blocks that contain information pertaining to each specimen. The header is at the beginning of the file and contains the original file name. Each specimen block has its own header (which is seven records long) and fifty data records (one for each experimental point on the loading path). The header for each specimen contains all the pertinent information associated with the corresponding specimen and the respective loading path. Fig. 11 presents a section of one of these files that corresponds to the second material of Table 1, i.e., graphite epoxy with AS1 fiber and 3501-6 resin with layup angle $+/-30°$. The fields in the data records, from left to right, are experimental point number, total dissipated energy D, boundary displacements (u_0,u_1, and u_2), and boundary forces (f_0,f_1, and f_2).

Another process called "GETABS" extracts the dissipated energy values from the afore mentioned file and stores them into files ready to be used from the resources available for the determination of the dissipated energy density function. All these processes were originally executed on a PRIME 750 minicomputer, but recently an effort has been undertaken to recast them in a more contemporary form on the NeXT cube computing platform, and have been recently ported to "Mathematica" code.

4. Total dissipated energy

The procedure for computing the energy dissipated internally in the specimen during an IPL test will be described. In what follows, the superscript $p = 1, \cdots, 50$ denotes an experimental point on a given loading path; $l = 1, \cdots, 15$ denotes a particular loading path; $r = 1,2$ denotes a particular test repetition; and subscript $i = 0,1,2$ denotes the components of the boundary forces and displacements.

4.1. Total energy

Consider first the total energy imparted to the specimen for each experimental point p as function of the boundary displacement vector $\boldsymbol{u}$. These energies, denoted as W^p, can be computed from the measured boundary forces and displacements by using the standard definition of mechanical work. Thus

$$W^p = W^p(\boldsymbol{u}) = \int_0^{\boldsymbol{u}^p} \boldsymbol{f}^p \cdot \mathrm{d}\boldsymbol{s}, \tag{1}$$

or in component form,

$$W^p = \int_0^{u_i^p} f_i^p \, ds_i = \int_0^{u_0^p} f_0^p \, ds_0 + \int_0^{u_1^p} f_1^p \, ds_1 + \int_0^{u_2^p} f_2^p \, ds_2. \quad (2)$$

Each term in Eq. (2) represents the energy stored in the specimen due to one of the measured force-displacement pairs (f_i^p, u_i^p) and is denoted by W_i^p. Hence, W^p can be expressed as the sum

$$W^p = W_0^p + W_1^p + W_2^p. \quad (3)$$

The integrals in Eq. (2) can be approximated using a discrete representation, i.e.,

$$W_0^p = \frac{1}{2} \sum_{a=1}^{p} (f_0^a + f_0^{a-1})(u_0^a - u_0^{a-1}),$$
$$W_1^p = \frac{1}{2} \sum_{a=1}^{p} (f_1^a + f_1^{a-1})(u_1^a - u_1^{a-1}), \quad (4)$$
$$W_2^p = \frac{1}{2} \sum_{a=1}^{p} (f_2^a + f_2^{a-1})(u_2^a - u_2^{a-1}),$$

or in general

$$W_i^p = \frac{1}{2} \sum_{a=1}^{p} (f_i^a + f_i^{a-1})(u_i^a - u_i^{a-1}),$$
$$\text{for } i = 0, 1, 2. \quad (5)$$

This approximation process is graphically depicted in Fig. 12 where the quantities in the summation are defined geometrically on a representative traction vs. displacement graph.

The area below the curve represents the energy W_i^p for loading up to point p as the sum of all trapezoids of area $\frac{1}{2}(f_i^a + f_i^{a-1})(u_i^a - u_i^{a-1})$. The total energy W^p can now be computed by substituting Eq. (5) into Eq. (3) and taking the sum of the three terms. Thus,

$$W^p = \frac{1}{2} \sum_{i=0}^{2} \sum_{a=1}^{p} (f_i^a + f_i^{a-1})(u_i^a - u_i^{a-1}),$$
$$\text{for } p = 1, 2, \cdots, 50. \quad (6)$$

Consider now the situation when the specimen unloads. Assume that when the specimen is unloaded proportionally from any point a of the curve in Fig. 12, the unloading occurs elastically along a line from the point a to the origin. This assumption is largely based on observations made during the early years of IPL use when unloading data were collected; it was found then that almost all specimens tested unloaded linearly and showed a maximum 2% permanent displacement set. These permanent displacements are likely a consequence of initial stresses introduced during manufacture and were deemed small enough to

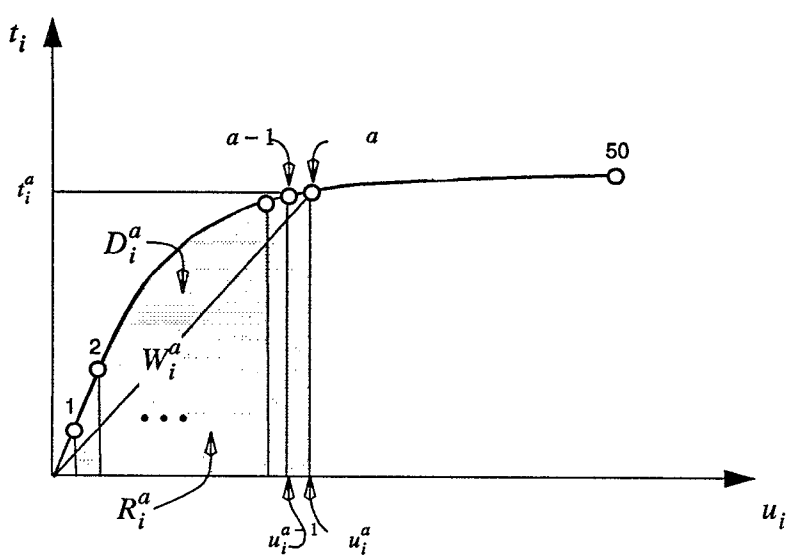

Fig. 12. Schematic representation of the integration scheme utilized for the computation of W_i^p as the sum of the rectangular slices under the load–displacement curve and of the energies associated with the loading of the specimen up to the point p.

ignore. This characteristic non-metal-like behavior during unloading has also been observed by other investigators [33] and it is currently attributed to the propensity of organic composites to form microcracks instead of flowing plastically.

4.2. Unloading

During unloading, a portion of the total energy W^p is recovered because of the elastic nature of the unloading response. This recoverable energy, denoted by a componentwise basis as R_i^p, is simply the triangular area under the line from a to the origin, or

$$R_i^p = \tfrac{1}{2} f_i^p u_i^p, \quad \text{for } p = 1, 2, \cdots, 50. \tag{7}$$

Knowing the available energies W_i^p and the recoverable energies R_i^p, it is a simple matter to compute the energy D^p dissipated in the specimen. Thus, on a componentwise basis, the energy dissipated in the specimen as it is loaded up to point p is simply the difference

$$D_i^p = W_i^p - R_i^p, \quad \text{for } p = 1, 2, \cdots, 50, \tag{8}$$

and, in graphical terms, is just the shaded area under the load-displacement line in Fig. 12. Substituting the expressions for the total and available energies from Eqs. (5) and (7) for each component i in the relation above, therefore, gives for D_i^p:

$$D_i^p = \frac{1}{2} \sum_{a=1}^{p} \left(f_i^a + f_i^{a-1}\right)\left(u_i^a - u_i^{a-1}\right) - \frac{1}{2} f_i^p u_i^p, \quad \text{for } p = 1, 2, \cdots, 50. \tag{9}$$

The total dissipated energy D^p (the energy which appears in the second column of the acquired data file shown in Fig. 11) can now be computed by summing D_i^p componentwise and results in

$$D^p = \frac{1}{2} \sum_{i=0}^{2} \sum_{a=1}^{p} \left(f_i^a + f_i^{a-1}\right)\left(u_i^a - u_i^{a-1}\right) - \sum_{i=0}^{2} \frac{1}{2} f_i^p u_i^p, \quad \text{for } p = 1, 2, \cdots, 50. \tag{10}$$

The dissipated energy computed this way can be considered to be a measured value since it is derived directly from measured quantities and the only sources of error are from the discrete numerical integration described and the quantization error of the data acquisition process. However, the very operation of integration also serves as a noise/error reduction methodology and works more in a beneficial rather than a detrimental manner in this case. To the authors' knowledge, these energy values represent the only attempt to measure dissipated energy caused by mechanical deformation in composite materials.

Table 2
Coordinates of load path unit vectors for each one of the 15 loading cases applied by the IPL.

Loading	a_0	a_1	a_2
1	0.000	−0.707	−0.707
2	0.000	−1.000	0.000
3	0.000	−0.707	0.707
4	0.500	−0.500	−0.707
5	0.707	−0.707	0.000
6	0.500	−0.500	0.707
7	0.707	0.000	−0.707
8	1.000	0.000	0.000
9	0.707	0.000	0.707
10	0.500	0.500	−0.707
11	0.707	0.707	0.000
12	0.500	0.500	0.707
13	0.000	0.707	−0.707
14	0.000	1.000	0.000
15	0.000	0.707	0.707

4.3. Evolution of displacements, tractions and dissipated energies

Fig. 13 is a graphical representation of the boundary displacements and tractions as well as the associated total and dissipated energies for the first specimen for loading path 11 for material AS1-30 (second row of Table 1). Loading path 11 does not have any rotation applied on the specimen as can be seen from Table 2 and from Fig. 9. This results in the apparent zeroing of the curve in Fig. 13(a.2), which consequently results in the blank energy graphs Figs. 13(c.2) and 13(d.2). However, due to the other two displacement components, there is a force reaction in the rotation direction as is shown in Fig. 13(b.2).

The dissipated energy curves start with values very close to zero and suddenly rise steeply. This

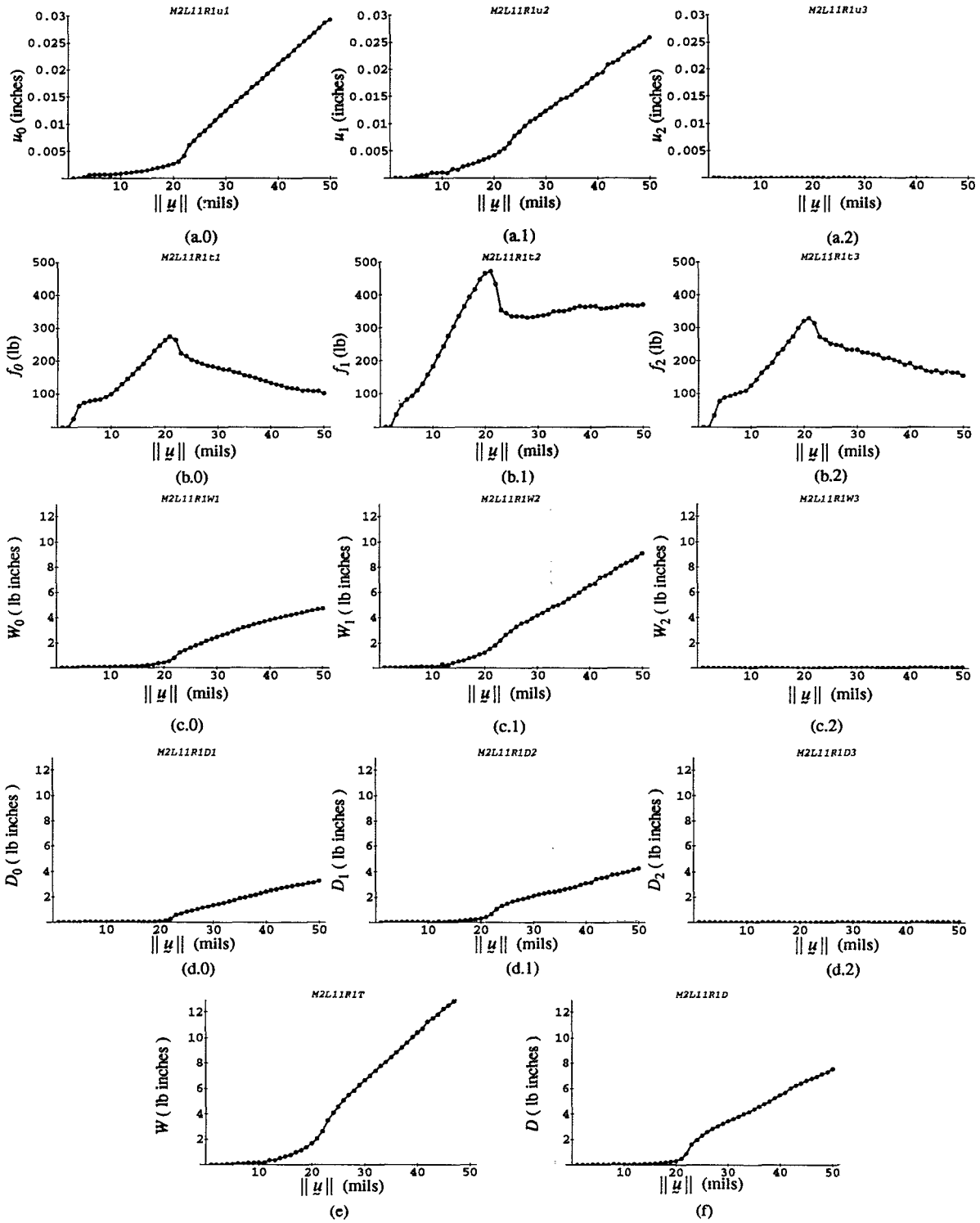
M2L11R1u1
M2L11R1u2
M2L11R1u3
u_0 (inches)
u_1 (inches)
u_2 (inches)
$\|\underline{u}\|$ (mils)
(a.0)
(a.1)
(a.2)
M2L11R1t1
M2L11R1t2
M2L11R1t3
f_0 (lb)
f_1 (lb)
f_2 (lb)
(b.0)
(b.1)
(b.2)
M2L11R1W1
M2L11R1W2
M2L11R1W3
W_0 (lb inches)
W_1 (lb inches)
W_2 (lb inches)
(c.0)
(c.1)
(c.2)
M2L11R1D1
M2L11R1D2
M2L11R1D3
D_0 (lb inches)
D_1 (lb inches)
D_2 (lb inches)
(d.0)
(d.1)
(d.2)
M2L11R1T
M2L11R1D
W (lb inches)
D (lb inches)
(e)
(f)

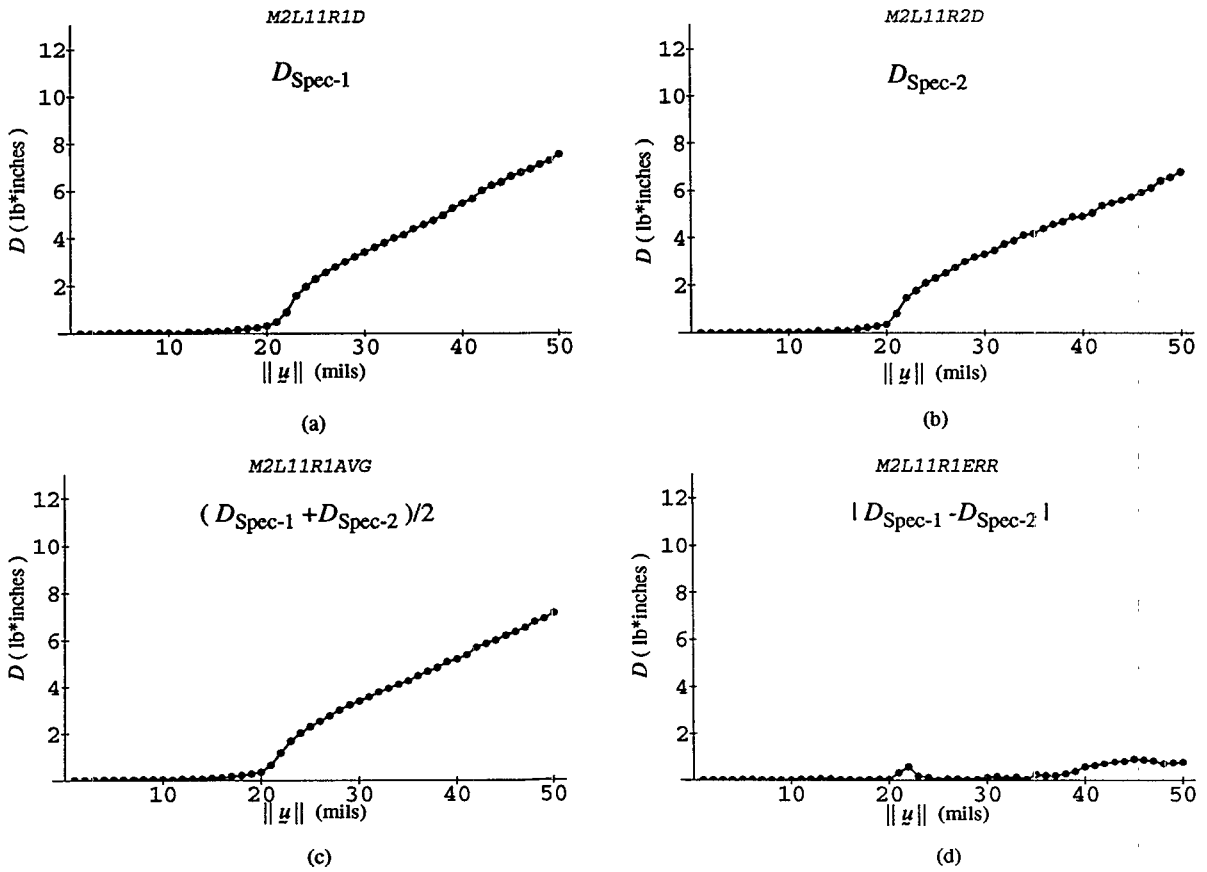

Fig. 14. Dissipated energies for specimen 1 (a), specimen 2 (b), their average value (c) and the absolute difference between the two (d), for material 2 (AS1, 6501-6, +/−30°) and loading path 11.

happens as the corresponding displacements exhibit an abrupt increase and the tractions reach a maximum value and then rapidly decrease. This point can be interpreted as defining a transition between purely linear elastic material behavior (i.e., no energy dissipation) and the point at which the material first exhibits nonlinear behavior with accompanying energy dissipation.

Summation of the energies for the three components in Figs. 13(c.0), 13(c.1), and 13(c.2) yields Fig. 13(e) for the energy absorbed from all three component combinations in the specimen. Similarly, summation of the dissipated energy components in Figs. 13(d.0), 13(d.1), and 13(d.2) yields the total energy lost in the specimen shown in Fig. 13(f). The morphology of the displacement, traction, and energy evolution curves for the rest of the loading paths is not necessarily identical to that of loading path 11.

To compare the repeatability of the process, Fig. 14 shows the dissipated energy evolutions for both specimens used on loading path 11 together

Fig. 13. Evolution of displacements (a.0, a.1, a.2), tractions (b.0, b.1, b.2), total absorbed energies (c.0, c.1, c.2), dissipated energies (d.0, d.1, d.2), total absorbed energy (e), and total dissipated energy (f), versus the magnitude of the experimentally imposed displacement vector $\| u \|$ of loading path 11 for the first specimen of material 2 (AS1, 3501-6, +/−30°).

with their average and absolute difference evolutions. As it seen in Fig. 14(d) the specimens behave almost identically. A small difference of the order of 12% appears at the last experimental point, very deep in the nonlinear region where the enormous amount of damage has made the material more unstable than it is in the linear region. The root mean square error (RMS) between the two values of the dissipated energy for the two specimens from the same material has never been found to exceed 5% for all materials tested.

An entire IPL test takes about 10 s, five of which are spent installing the specimen in the grips. As a result, the specimen testing rate can be 360 specimens/hour. At this rate, data can be collected for 12 different materials per hour. The overall daily production rate for an 8-hour day is, therefore, 960 specimens, or 96 different materials, or 24 materials systems (since we use 4 layup angle combinations for each fiber–resin combination). The total number of experimental points per fiber-resin combination is 6000. Each loading path corresponds to 2.4 KB of data while 288 KB are acquired for each material system. The daily throughput capacity of the acquisition process approaches 20.74 MB/day.

A spatial map of the absorbed energy density over the specimen for each experimental point can be identified by using the simulating capability described in Part II [31]. Fig. 15 shows the evolution of the dissipated energy distribution for the experimental points corresponding to 20%, 40%, and 60% of the total load (points 10, 20, and 30) in association with the total dissipated energy evolution curve for the specimen associated with loading path 11, repetition 1. These distributions were obtained by using the structural simulator described in Part II. In these distributions, the darker the shade of gray, the higher the value of the dissipated energy density. From this figure it can be deduced that for the low load level corresponding to 20% of the total, the total dissipated energy evolution curves shows that almost the entire specimen is in the linear region because of the very small value of the dissipated energy, and the corresponding distribution shows indeed that only a very small region on the upper right corner entered into the nonlinear domain with very small values. As the load

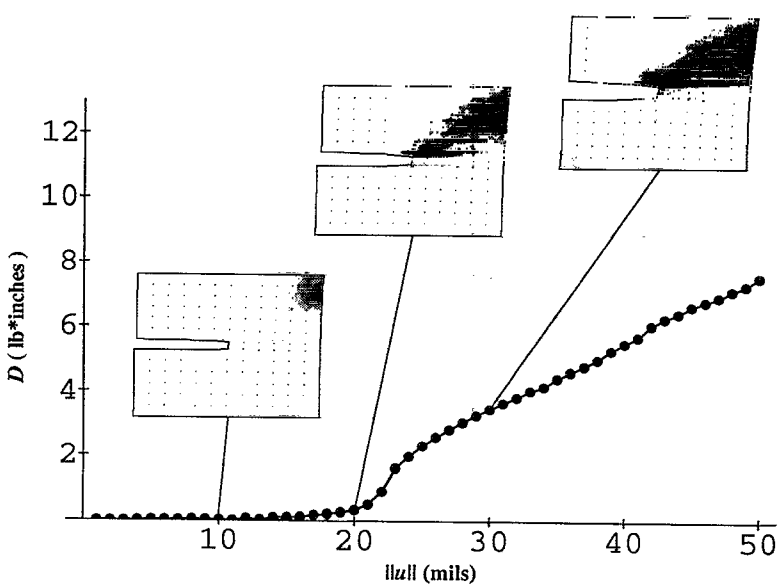

Fig. 15. Distributions of dissipated energy for 20%, 40%, and 60% of the total loading, associated with corresponding the total experimentally measured dissipated energy for the first specimen of loading path 11.

increases, the total dissipated energy of the specimen increases and, as expected, more areas in the specimen enter into the nonlinear region, while the old ones intensify their absorption levels.

5. Computational procedures

The right and lower subpaths in Fig. 1 represent the flow of activities related to the determination of the dissipated energy density function ϕ. It is important, however, to clarify the range of hypotheses and assumptions employed in the present analysis to illustrate how the procedure relates to the so-called inverse approach.

5.1. Data processing

Fig. 16 describes the computational process used to obtain the dissipated energy density function in terms of its evaluation on discrete points over the strain space. A user interface that controls all interprocess and intercomputer communication is the mechanism by which the user controls the overall process. The "PATRAN" solid modeling package is used to define the geometry, material, and loading specifications for the finite element model of the specimen structure, which in turn is fed into the "ABAQUS" finite element code via the "PATABA" format translator. The output from the linear strain analysis from "ABAQUS" is then translated from "ABAPAT" into files containing the strain and displacement distributions for the corresponding loading cases that are displayable by "PATRAN." The "ABSPAT" module developed at NRL then

- uses the analysis results for all the loading cases as well as the experimentally measured values of the dissipated energy from the files discussed in Section 3.5 to synthesize the quantities necessary for estimating the 125 coefficients that describe the dissipated energy function,
- carries out the estimation, and
- generates one file per material system that contains the 125 coefficients.

5.2. Strain field

The measured absorbed energy is a function of specimen geometry, loading condition, and material. To factor out the influence of specimen geometry and loading and to obtain a dissipated

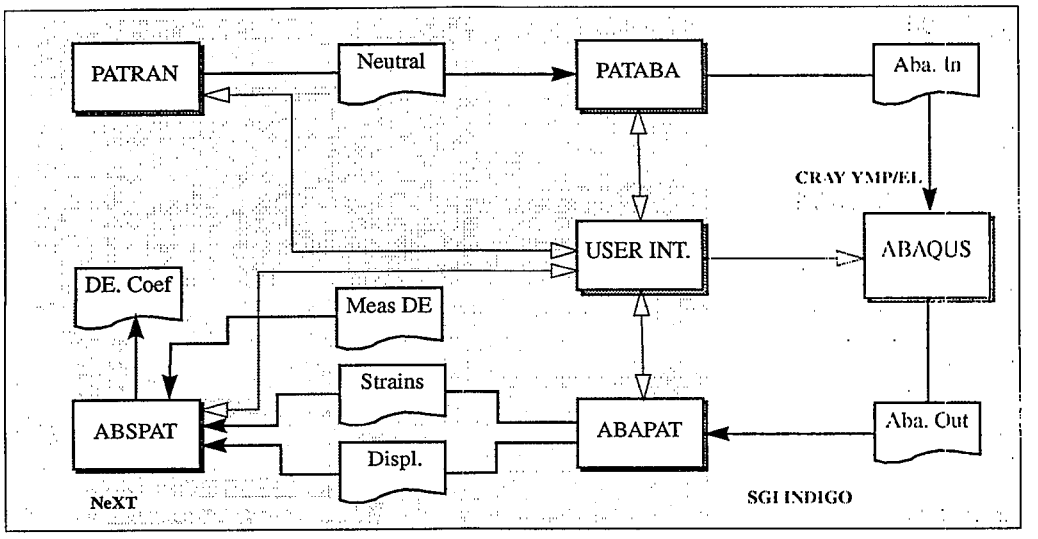

Fig. 16. Block diagram of the modules used to compute the dissipated energy coefficients for each material, along with the computational resources utilization.

energy function that depends solely on the material, it is necessary to develop a deconvolution procedure. Consider a structure with geometry s, consisting of a particular material m, and under a specific loading condition l. A strain state exists at any point described by the position vector $\boldsymbol{x}$. The strain vector $\boldsymbol{\varepsilon}$ corresponding to this state with the classical in-plane components (ε_{xx}, ε_{yy}, and ε_{xy}) is a function of s, m, l, and $\boldsymbol{x}$; i.e.,

$$\boldsymbol{\varepsilon} = \boldsymbol{\varepsilon}(s, l, m, \boldsymbol{x}). \tag{11}$$

For a specific specimen, a subscript 0 will be used to denote the corresponding geometry and material as S_0 and m_0, respectively. It will become evident from the analysis that the strain field for each one of the loading cases needs to be determined. In the ideal case, these fields should be experimentally measured along with boundary tractions and displacements in the IPL tests. This will be a feature of the new generation of NRL's automated loading machines; however, the current generation has no such capabilities. The results and analysis presented here are based on an alternative approach. More specifically, reference is made to estimate the strain field by discretizing the geometry of the specimen into 150 elements as shown in Fig. 17. Apply the loading and boundary conditions by the IPL on the specimen, and compute the in-plane strains by running an appropriate number of linear elastic finite element analyses using the code "ABAQUS". The selection of the linear analysis was based on the fact that in very few of the experiments were specimens observed to fail in a way that would indicate that very large amounts of energy had been dissipated by internal material damage. The initial purpose was to establish an analytical tool based on experimental evidence for predicting the onset of nonlinear response and an approximation of this response, rather than the exact nonlinear material behavior. The three strain components corresponding to the centroids of the elements of the specimen structure s_0 were stored in files organized according to loading case. For practical purposes, instead of running 15 loading cases (one for each loading path), only the cases corresponding to the loading paths (1, 0, 0), (0, 1, 0), and (0, 0, 1) corresponding to pure shear, opening, and rotation displacements, respectively, were run. This was because all other cases could be synthesized by linear superposition.

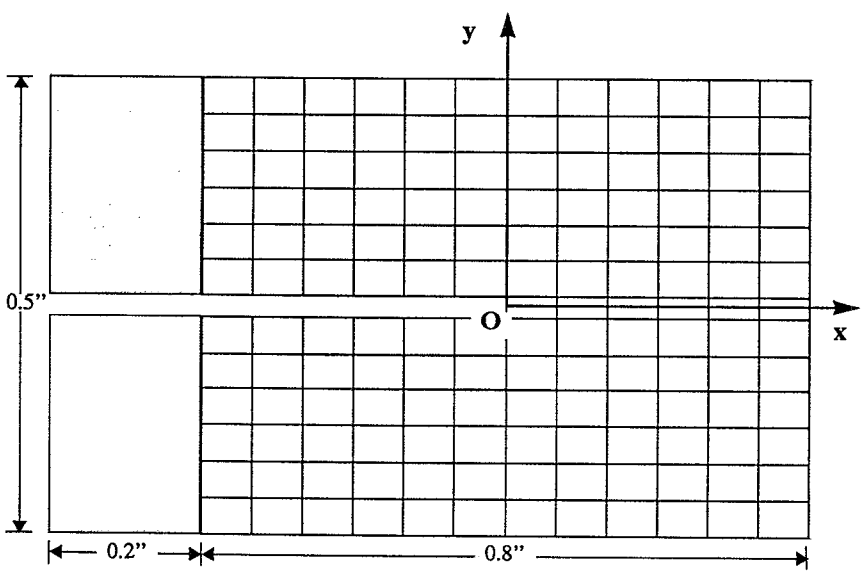

Fig. 17. Mesh for the view area of the specimen.

5.3. Dissipated energy density function

Let ϕ denote the dissipated energy density per unit of volume of material. It depends on the strain vector $\boldsymbol{\varepsilon}$ and the material, i.e., ϕ $(\boldsymbol{\varepsilon}, m)$. This function can be one of an arbitrarily large set of functions. For computational efficiency, we assume that the effect of the material and strain dependence can be decomposed by an appropriate choice of form for this function. This can be done by selecting a form expressed in terms of a set of coefficients that depend solely on the material properties, and a set of constant basis functions. For simplicity, the following linear combination case is selected:

$$\phi(\boldsymbol{\varepsilon}, m) = \phi(\boldsymbol{\varepsilon}, \boldsymbol{c}) = c_1(m)\chi_1(\boldsymbol{\varepsilon}) + \cdots + c_m(m)\chi_n(\boldsymbol{\varepsilon}) = c_i(m)\chi_i(\boldsymbol{\varepsilon}). \tag{12}$$

In this form, $\boldsymbol{c}$ represents the vector of the material depended coefficients c_i, and χ_i represents the basis functions depending only on strains $\boldsymbol{\epsilon}$ and defined at a total of n distinct points distributed over the strain space. Eq. (12) can be thought of as being an interpolation function

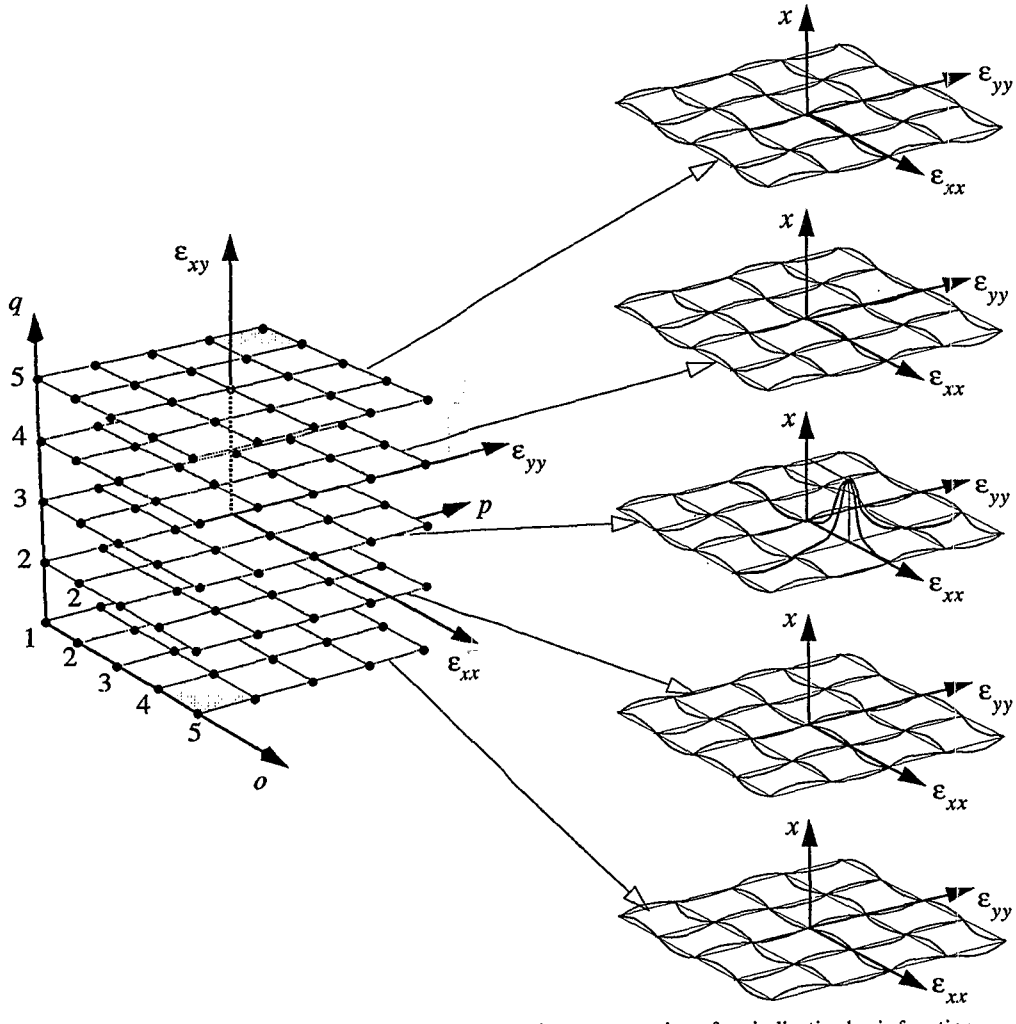

Fig. 18. Strain space representation and characteristic representation of an indicative basis function.

allowing evaluation of ϕ on points other than the ones used to define the basis functions.

For the case under discussion, 125 (i.e., 5 per axis) such points were selected to be uniformly distributed in the Cartesian representation of the components of the strain space. Fig. 18 shows the cuboidal distribution of the points where the basis function for our case is defined. To have a unique number characterizing each one of the points where the strains are evaluated, three indices o, p, and q have been chosen along the $\varepsilon_{xx}, \varepsilon_{yy}, \varepsilon_{xy}$ axes, respectively, to count from 1 to 5 as the (opq) frame of reference indicates in Fig. 18. This resulted in using a counter i for the points associated with these indices in the following relationship:

$$i = o + 5(p-1) + 25(q-1) \quad \text{for } o, p, q = 1, \cdots, 5. \tag{13}$$

The increments along the three orthogonal strain component directions in this space are equidistanced and the step is the quotient of the maximum value for any of the strains obtained from the finite element analysis of the structure under consideration divided by 4 (number of spaces between the discrete points of evaluation). The basis functions have the property of being equal to the value of the function at the evaluation point (in this case, 1), and zero at any other evaluation point of their domain. A consequence of this is that the value of the function ϕ according to Eq. (12) at an evaluation point is equal to the coefficient of the basis function for that point. This, it turns out, is a very convenient feature for the solution scheme described later in this section.

Fig. 18 gives a graphic definition of how a basis function behaves. The five successive planes have been shifted out of the strain space and have been drawn such that the vertical axis represents the value of the function χ. The function has been evaluated at the point defined by ($o = 4$, $p = 3$, $q = 3$), or ($i = 64$), and, as can be seen, the value of the function is zero at all nodal points of the strain space except for the point where it evaluates to 1. There it remains the same regardless of the evaluation point. By letting ε_i signify the strain vector for each point i for all 125 labeled points in the strain space, the basis functions with these properties can be expressed as:

$$\chi_i(\varepsilon_j) = \begin{cases} 1, & i = j \\ 0, & i = j \end{cases} \quad \text{for } i, j = 1, 2, \cdots, 125. \tag{14}$$

Introducing this relation to Eq. (12), for one of these points i there results

$$\begin{aligned} \phi(\varepsilon_i, m) &= c_1(m)\chi_1(\varepsilon_i) + \cdots + c_i(m)\chi_i(\varepsilon_i) \\ &\quad + \ldots + c_m(m)\chi_n(\varepsilon_i), \\ \phi(\varepsilon_i, m) &= c_1(m)0 + \cdots + c_i(m)1 \\ &\quad + \cdots + c_m(m)C, \end{aligned} \tag{15}$$

which after evaluation yields:

$$\phi(\varepsilon_i, m) = c_i(m). \tag{16}$$

Thus, Eq. (12) may be viewed as an interpolation function that linearly determines the value of the dissipated energy density function at any point in the strain space as long it lies in the cuboidal region spanned by the 125 points. The problem of determining the analytical expression for ϕ is now reduced to determining the coefficients c_i, such that the family of functions represented by Eq. (12) is restricted to one which represents a "best fit" of experimental data.

The total energy Φ dissipated throughout the volume of the structure under consideration (s_0) for each loading condition l_0 can be computed as the volume integral of the dissipated energy function over the spatial extent of the structure:

$$\Phi = \int_{\partial s_0} \phi(\varepsilon, c)\, \mathrm{d}x. \tag{17}$$

By virtue of Eq. (12), this relation reduces to

$$\begin{aligned} \Phi &= \int_{\partial s_0} (c_1(m)\chi_1(\varepsilon(l_0, x)) \\ &\quad + \cdots + c_m(m)\chi_n(\varepsilon(l_0, x)))\, \mathrm{d}x \\ &= \int_{\partial s_0} c_i(m)\chi_i(\varepsilon(l_0, x))dx. \end{aligned} \tag{18}$$

Assuming that D represents an experimentally obtained value of the total dissipated energy for a given structure s_0 and a given loading condition

l_0, there is an appropriate selection of the coefficients c_i such that the value obtained from Eq. (18) approximates this measured value. This can be expressed by

$$\Phi(s_0, l_0) + e = D(s_0, l_0), \tag{19}$$

where e expresses the error between the two values of the dissipated energy.

5.4. Solution and optimization scheme

For the case of the particular specimen geometry s_0 and the particular loading case that corresponds to a corresponding experimental point p, the integral of Eq. (18) can be equivalenced by a discretized form indicating the sum of the dissipated energy of each of the 150 elements of the specimen structure. Eq. (19) can now be rewritten as:

$$\sum_{e=1}^{150} c_i \chi_i(\varepsilon_e^p) V_e^p + e^p = D^p, \tag{20}$$

where V_e^p represents the volume of the element e for the loading point p. Since this represents one of many relations, it follows that different increments of the index 1 corresponding to different loading conditions, the set of these relations can be represented in a matrix form:

$$[X]\mathbf{c} + \mathbf{e} = \mathbf{d}, \tag{21}$$

where [X], **c**, and **d** matrices have elements described by $\chi_{ip} = \sum_{e=1}^{150} \chi_i(\varepsilon_e^p) V_{e,c_i}^p$ and d respectively. We selected third point from each loading path (17 experimental points per loading path) for all 15 loading paths for a total of 255 experimental points, and **d** is constructed as follows:

$$\mathbf{d}^{\mathrm{T}} = \left[[\mathbf{D}_1^p]^{\mathrm{T}}, \ [\mathbf{D}_2^p]^{\mathrm{T}}, \cdots, [\mathbf{D}_l^p]^{\mathrm{T}}, \cdots, [\mathbf{D}_{15}^p]^{\mathrm{T}} \right], \tag{22}$$

with $p = 1,4,\ldots,49$, where

$$[\mathbf{D}_l^p]^{\mathrm{T}} = \left[D_l^1, D_l^4, D_l^7, \cdots, D_l^{49} \right], \tag{23}$$

where the elements are obtained from Eq. (10) for each loading path l.

Eq. (21) represents an overdetermined system of 255 equations with 125 unknowns. However, the requirement that the dissipated energy is a monotonically increasing function of the strains imposes a new set of constraints that can be now be expressed in the following inequality:

$$[M]\mathbf{c} \geq 0. \tag{24}$$

The array [M] has 125 columns and 100 rows, since it represents a tuple of 100 additional constraints. It is defined as:

$$[M] = \begin{bmatrix} \mathbf{M}_1^{\mathrm{T}} \\ \mathbf{M}_2^{\mathrm{T}} \\ \cdots \\ \mathbf{M}_{100}^{\mathrm{T}} \end{bmatrix}, \tag{25}$$

where $\mathbf{M}_c^{\mathrm{T}}$ for $c = 1,\ldots,100$ are row matrices corresponding to each one of these constraints.

Thus the problem of determining the 125 coefficients c_i is reduced to the solution of Eq. (21) under the inequality constraints in Eq. (24). This combination provides a total of 355 relations, and it represents a classical optimization problem with inequality constraints where the objective is to minimize the function (objective function) $\|\mathbf{e}\|$ such that both Eqs. (21) and (24) are satisfied. This is a standard problem in quadratic programming and is readily solved using well-established numerical techniques [34]. A vector space graphical representation of the entities involved in the optimization scheme can be found in the Appendix.

In light of the preceding considerations, the dissipated energy is now fully determined at all 125 points of the strain space since, as discussed previously, the computed coefficients represent the values of the dissipated energy at those points. The dissipated energy can, therefore, now be computed at any point in any material that has been tested. The strains determine the particular subregion in the cube spanning the strain space, such that a linear interpolation performed between the values of the dissipated energy at the surrounding point establishes the value of the dissipated energy at the intermediate point.

6. Conclusions

In conclusion, an approach is formulated to characterize failure behavior and degree of load

induced internal damage in composite materials and structures. This approach is based on a systematic experimental procedure to observe response of composite materials subjected to multiaxial load environment. The energy dissipated by internal failure mechanisms is used as a measure of internal damage and is characterized by an energy dissipation function, which is determined by means of a deconvolution procedure using data provided by NRL's automated In-Plane Loader.

Use of this information as a failure analysis and prediction tool is demonstrated by simulating the structural response of some naval structural components made from several different composite materials. Part II [31] of this work will display the dissipated energy density distributions in composite specimens and naval structures alike.

Part III [32] will present a general theory that includes the derivation of the constitutive behavior of damaged composites.

Appendix: A vector space representation of the optimization scheme

A vector space geometrical representation of the optimization scheme provides for a simple explanation of the optimization procedure. Assume for the sake of simplicity (and because we cannot represent entities having dimensions higher than three on paper) that the quantity $[X]\mathbf{c}$ can be represented as a vector $\boldsymbol{c}$ in a two-dimensional space X with X_1 and X_2 being the corresponding basis vectors as shown in Fig. 19. The columns of the array $[X]$ contain the components of the basis vectors X_1 and X_2 in terms of a higher dimensional space D, the higher dimensions of which are denoted by the axis N normal to the space X.

Assume now that another vector $\boldsymbol{d}$ lies in the higher dimensional space D of which the space X is a subspace. The difference of these two vectors then lies in this higher dimensional space and is another vector denoted as $\boldsymbol{e}$ which expresses the error between the two vectors, so that

$$\mathbf{e} = \mathbf{d} - \mathbf{c}. \tag{26}$$

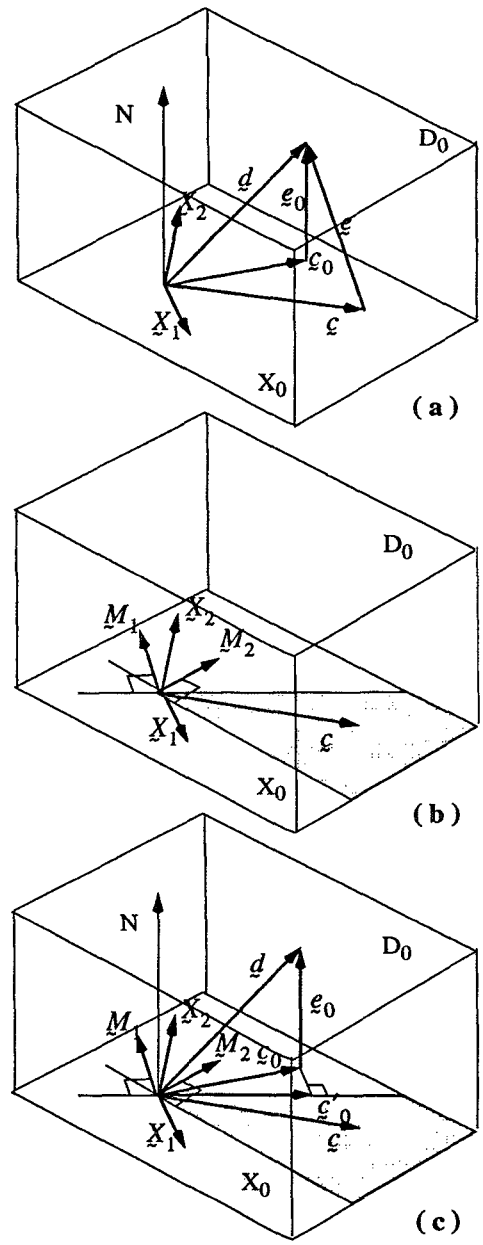

Fig. 19. Geometrical representation of the optimization procedure describing (a) the solution for Eq. (C2), (b) for the constraints, and (c) for both equation and constraints.

This can be rewritten in the matrix form

$$[X]\mathbf{c} + \mathbf{e} = \mathbf{d}. \tag{27}$$

The objective of the process is to determine a vector c_0 such as the magnitude (or norm) of the vector e takes its minimum value e_0 according to

$$\min \| e \| = e_0. \tag{28}$$

In the case of the usual Euclidean norm, i.e., the square root of the sum of the squares of the components, c_0 turns out to be the projection of the vector d of space D onto the space X, and therefore c_0 is normal to this space.

Fig. 19(b) deals with the effects of inequality constraints case. Suppose M_1, M_2 are the vectors corresponding to the matrices $\mathbf{M}_1^{\mathrm{T}}$ and $\mathbf{M}_2^{\mathrm{T}}$, which also lie in the space X. Then, the inequality constraint of the form

$$[M]\mathbf{c} \geq 0 \tag{29}$$

specifies that the only acceptable solutions for c must lie in the region of X (shaded region) defined by the interior of the two lines which also lie in X and are normal to the vectors M_1, M_2 respectively.

However, as can be seen in Fig. 19(c), the vector c_0, which exactly satisfies Eq. (22) and minimizes e to a value e_0, may lie outside the region specified by the constraints. In this case the quadratic programming methodology determines a vector c_0', which satisfies the constraints by being the projection of c_0 onto the closest boundary of the shaded region. The magnitudes of the components of c_0' in the space X will then be the desired coefficients c_i. Finally, this process is valid when the spaces X and D have arbitrary dimensions so long as $\mathrm{Dim}(X) \leq \mathrm{Dim}(D)$ and so obviously applies in this case.

Acknowledgements

The authors wish to acknowledge past and current financial support of the following Navy organizations and the indicated program managers:
Office of Naval Technology (J.J. Kelly [3] and I.L. Caplan [3] (DTRC Block Manager));
Strategic Systems Project Office (E.L. Throckmorton[3], R. Kinert, and F. Vondersmith);
Naval Air Systems Command (C.F. Bersch);
Naval Sea Systems Command (H.H. Vanderveldt, C. Zanis, W.R. Graner, and T.F. White).

The authors also wish to acknowledge helpful technical discussions with H. Marshall, Lockheed Palo Alto Research Laboratory, and J. Pitman, Gibbs and Cox Inc.

[3] Current Program Managers.

References

[1] R. Badaliance and H.D. Hill, Damage mechanisms and life prediction of graphite/epoxy composites, in: *STP775 Damage in Composite Materials*, ed. K.L. Reifsnider, ASTM (Philadelphia, PA, 1982) pp. 229–242.

[2] G.E. Morris and C.M. Hetter, Fractographic studies of graphite/epoxy fatigue specimens, in: *STP775 Damage in Composite Materials*, ed. K.L. Reifsnider, ASTM (Philadelphia, PA, 1982) pp. 27–39.

[3] J.E. Masters and K.L. Reifsnider, An investigation of cumulative damage development in quasi-isotropic graphite/epoxy, in: *STP775 Damage in Composite Materials*, ed. K.L. Reifsnider, ASTM (Philadelphia, PA, 1982) pp. 40–62.

[4] A. Highsmith and K.L. Reifsnider, Stiffness-Reduction Mechanisms in Composite Laminates, in: *STP775 Damage in Composite Materials*, ed. K.L. Reifsnider, ASTM (Philadelphia, PA, 1982) pp. 103–117.

[5] J. Aveston and A. Kelly, Theory of multiple fracture of fibrous composites, *J. Material Science* 8, 352–362 (1973).

[6] S.W. Tsai and H.T. Hahn, On the behavior of composite laminates after initial failures, *J. Composite Materials* 8, 288–305 (1974).

[7] K.L. Reifsnider and W.W. Stinchcomb, Fatigue damage mechanisms in composite materials: A review, *Symp. on Basic Mechanisms of Fatigue*, ASTM, 1978, Kansas City, Missouri, 1978, pp. 762–787.

[8] K.L. Reifsnider, Fatigue behavior of composite materials, *Int. J. Fracture* 16, 563–583 (1980).

[9] G.J. Dvorak and W.S. Johnson, Fatigue of metal matrix composites, *Int. J. Fracture* 16, 585–607 (1980).

[10] B.A. Bilby, R. Bullough and E. Smith, Continuous distributions of dislocations: a new application of the methods of non-riemannian geometry, *Proc. R. Soc. London A* 231, 263–273 (1955).

[11] O.W. Dillon, Jr. and J. Kratochvil, Thermodynamics of elastic-plastic materials as a theory with internal state variables, *J. Appl. Physics* 40, 3207–3218 (1969).

[12] L.M. Kachanov, On the creep fracture time, Izv. AN SSR, Otd. Tekhm. Nauk. 8 26 (1958).

[13] D.H. Allen, C.E. Harris and S.E. Groves A thermomechanical constitutive theory for elastic composites with distributed damage-i and ii, *Int. J. Solids Structures* 23, 1301–1338 (1987).

[14] Z.P. Bazant, Mechanics of distributed cracking, *Appl. Mech. Rev.* 39, 675–705 (1986).

[15] L.M. Kachanov, *Introduction to Continuum Damage Mechanics* (Martinus Nijhoff, Dordrecht, 1986).

[16] D. Krajcinovic, Continuum damage mechanics, *Appl. Mech. Rev.* 37, 1 (1984).

[17] D. Krajcinovic, Update to continuum damage mechanics, *Appl. Mech. Update*, LW3 (1986).

[18] J. Lemaitre, Formulation and Identification of Damage Kinetic Constitutive Equations, in: *CISM Courses and Lectures* No. 295 (Springer, Wien, 1987) p. 37.

[19] E.T. Onat and F.A. Leckie, Representation of mechanical behavior in the presence of changing internal structure, *J. Appl. Mech.* 55, 1 (1988).

[20] R. Talreja, *Fatigue of Composite Materials* (Technomic, Lancaster, PA, 1987).

[21] R.A. Schapery, Deformation and fracture characterization of inelastic composite materials using potentials, *Polymer Eng. and Sci.* 27(1), 63–76 (1987).

[22] R.A. Schapery, Mechanical characterization and analysis of inelastic composite laminates with growing damage, in: *Mechanics of Composite Materials*, ASME AMD, No. 2 (1989) pp. 1–9.

[23] R.A. Schapery, A method for mechanical state characterization of inelastic composite laminates with damage, in: *Advances in Fracture Research, Proc. 7th Int. Conf. on Fracture*, Vol. 3 (1989) pp. 2177–2189.

[24] R.A. Schapery, A theory of mechanical behavior of elastic media with growing damage and other changes in structure, *J. Mech. Phys. Solids* 38(2), 215–253 (1990).

[25] J.G. Michopoulos, G.C. Sih, S.C. Chou and J.F. Dignam, Energy dissipation in highly compressed cylindrical bar specimens, *J. Theoret. and Appl. Fracture Mech.* 2(2), 105–110 (1984).

[26] G.C. Sih, Thermal/mechanical interaction associated with the micromechanisms of material behavior, Institute of Fracture and Solid Mechanics, Lehigh University, Bethlehem, PA, 1987.

[27] G.C. Sih, D.Y. Tzou and J.G. Michopoulos, Secondary temperature fluctuation in cracked 1020 steel specimen loaded monotonically, *J. Theoret. and Appl. Fracture Mech.* 7(2), 74–87 (1987).

[28] P.W. Mast, L.A. Beaubien, M. Clifford, D.R. Mulvile, S.A. Sutton, R.W. Thomas, J. Tirosh and I. Wolock, A semi-automated in-plane loader for material testing, *Experimental Mechanics* 23(2), 236–241 (1983).

[29] P.W. Mast, L.A. Beaubien, D.R. Mulville, S.A. Sutton, R.W. Thomas, J. Tirosh and I. Wolock, Failure criteria for composite structures in high performance composites and adhesives for V/STOL aircraft, ed. C.F. Poranski, NRL Memorandum Report 5231, Washington, DC (1984) pp. 59–90.

[30] P.W. Mast, G.E. Nash, J.G. Michopoulos, R.W. Thomas, R. Badaliance and I. Wolock, Experimental determination of dissipated energy density as a measure of strain-induced damage in composites, NRL Report NRL/FR/6383-92-9369 (April 17, 1992).

[31] P.W. Mast, G.E. Nash, J.G. Michopoulos, R. Thomas, R. Badaliance and I. Wolock, Characterization of strain-induced damage in composites based on the dissipated energy density: Part II. Composite specimens naval structures, this issue, *J. Theor. and Appl. Fract. Mech.* 22, 97–114 (1995).

[32] P.W. Mast, G.E. Nash, J.G. Michopoulos, R. Thomas, R. Badaliance and I. Wolock, Characterization of strain-induced damage in composites based on the dissipated energy density: Part III. General material constitutive relation, this issue, *J. Theor. and Appl. Fract. Mech.* 22, 115–125 (1995).

[33] M.J. Lamborn and R.A. Schapery, An investigation of deformation path-independence of mechanical work in fiber-reinforced plastics, Proc. 4th Japan–U.S. Conf. on Composite Materials, 1988, Technomic, Washington DC (1988) pp. 991–1000.

[34] P.E. Gill, W. Murray and M.H. Wright, *Practical Optimization* (Academic Press, London, 1981).